nature communications

Article

https://doi.org/10.1038/s41467-026-70322-5

Electric double layer structure in concentrated aqueous solution

Received: 19 July 2025

Accepted: 24 February 2026

Published online: 07 March 2026

Check for updates

Minho M. Kim[1,4], Dong Hyun Kim[2,4], Junsic Cho[2,4], Seung-Jae Shin[3] ✉, Chang Hyuck Choi[2] ✉ & Hyungjun Kim[1] ✉

Toward tailored electrocatalysis, significant attention has been directed to the electrode-electrolyte interface. The electric double layer provides a crucial microenvironment for electrochemical reactions. However, its atomic-scale structure remains unresolved, particularly for non-dilute electrolyte concentrations relevant to practical systems. A notable example is the camel-to-bell shape transition in the capacitance curve, where two peaks merge as the concentration increases, which is still poorly understood at the molecular level. Herein, using all-atom simulations, we elucidate the electric double layer structures and their phase transitions which give rise to capacitance peaks. The predicted transition potentials match the experimental peak positions. We observe collective water reorientation in the cathodic region and anion surface condensation in the anodic region, which are further validated by in situ spectroscopy. Finally, we construct an electric double layer structural phase diagram to provide detailed insight into the electric double layer microenvironment. This work presents a valuable framework for design of improved interfaces.

The electric double layer (EDL), which is formed at electrochemical interfaces when the electrolyte region screens a charged electrode, is one of the most fundamental concepts in electrochemistry[1,2]. Because electrochemical reactions occur within the EDL, understanding its structure and behaviour is directly relevant to the electrocatalytic performance. In particular, optimisation of the EDL structure for tuning of the local microenvironment has gained significant attention as a strategy for the development of high-performance electrocatalysts, especially for key reactions related to sustainable technologies, such as electrochemical CO_2 reduction and hydrogen evolution[3–25].

Nevertheless, the atomic-scale structure of the EDL remains largely elusive, particularly under a finite bulk concentration (e.g., 0.1–1 M), which is the condition most representative of practical electrochemical operations. The EDL structure is primarily defined by water orientation and local ion concentration (Fig. 1a), both of which contribute to charge storage at the interface in response to an applied potential difference across the EDL, E. Consequently, the change in the stored interfacial charge density, σ, with respect to the changes in E reflects the underlying structural details of the EDL, while the differential capacitance, defined as $C = \partial\sigma/\partial E$, serves as a sensitive fingerprint of EDL structure.

The camel-to-bell shape transition is a characteristic feature observed in the EDL capacitance curve when the bulk electrolyte concentration is increased from the very dilute to finite regime[26–30]. When measuring the capacitance of an interface composed of a single-crystal electrode (e.g. silver) and an aqueous electrolyte containing non-specifically adsorbing ions (e.g. NaF electrolyte), a two-peak (camel-shaped) curve shifts to a single-peak (bell-shaped) curve with increasing concentration. Starting with the traditional Gouy-Chapman-Stern (GCS) theory[31–33], various theories have been proposed to explain this transition. However, these theories have failed to explain the peak behaviour (Supplementary Fig. 10), and have been mostly based on

[1]Department of Chemistry, Korea Advanced Institute of Science and Technology (KAIST), Daejeon, Republic of Korea. [2]Department of Chemistry, Pohang University of Science and Technology (POSTECH), Pohang, Republic of Korea. [3]School of Energy and Chemical Engineering, Ulsan National Institute of Science and Technology (UNIST), Ulsan, Republic of Korea. [4]These authors contributed equally: Minho M. Kim, Dong Hyun Kim, Junsic Cho.
✉e-mail: seungjae.shin@unist.ac.kr; chchoi@postech.ac.kr; linus16@kaist.ac.kr

https://doi.org/10.1038/s41467-026-70322-5

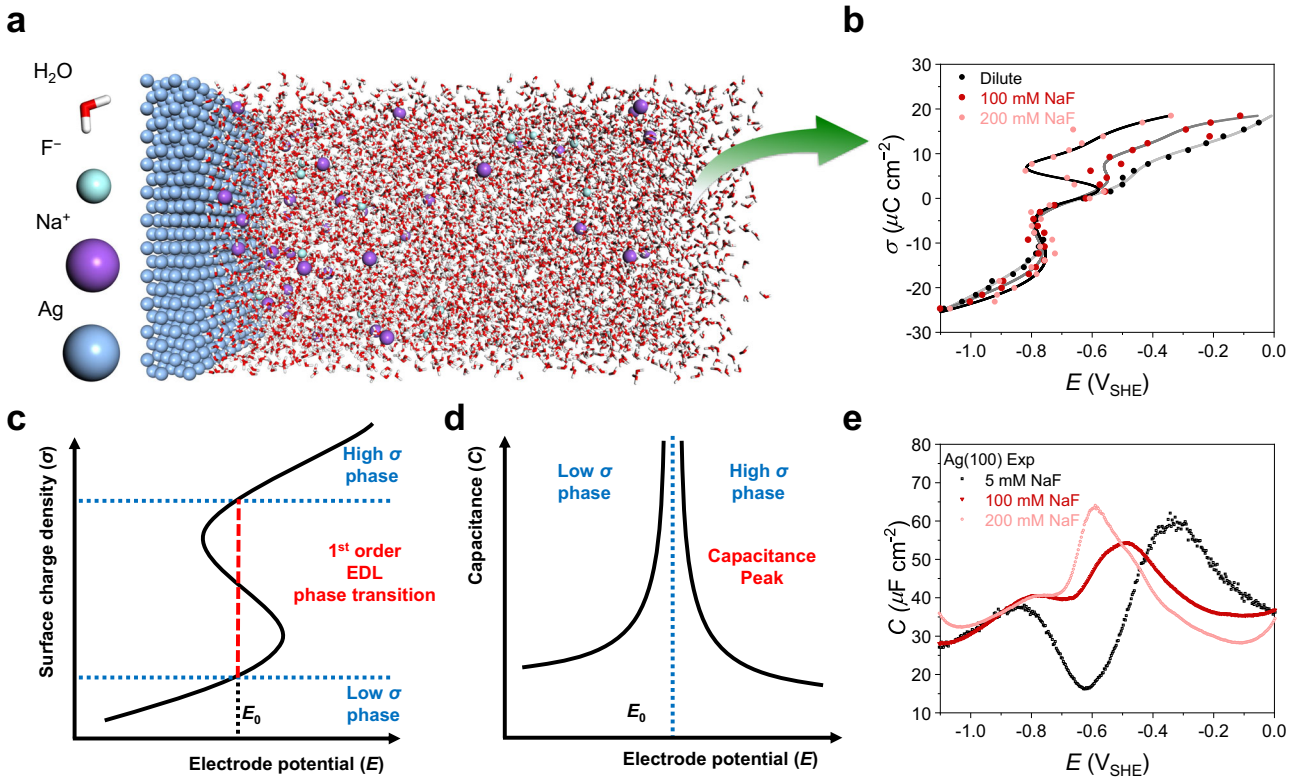

Fig. 1 | Phase transitions predicted from all-atom EDL simulations and their connection to capacitance peaks. a Snapshot of the simulation system for the Ag(100) electrode–NaF electrolyte interface. **b** Curves for surface charge density (σ) versus electrode potential (E) predicted from all-atom simulations at different bulk electrolyte concentrations. Red ovals indicate S-shaped regions associated with phase transitions. **c** Schematic diagrams showing the S-shaped curve on the σ-E plane, with the red dashed line indicating the phase transition path. **d** Corresponding schematic of the capacitance peak. **e** Experimental capacitance curves for the Ag(100) electrode in NaF electrolytes at 298 K, showing the camel-to-bell shape transition with increasing electrolyte concentration.

mesoscopic to macroscopic models[30,34–36]. For example, Kornyshev introduced a lattice gas model that accounts for the steric effects among ions[34]. This model predicts the merging of the two peaks when the capacitance decreases owing to ion saturation at high bias potentials; however, it is mainly applicable to highly concentrated electrolytes with large ion sizes, such as ionic liquids, rather than to aqueous electrolytes.

Modern atomic-level simulations serve as computational microscopes for EDL structure exploration. Using ab initio molecular dynamics (AIMD) simulations of the Pt(111)-water interface, Cheng et al. proposed that the bell-shaped Helmholtz capacitance curve originated from water adsorption[37]. Later, the Koper group combined their simulation results with the Gouy-Chapman (GC) model to reproduce the camel-to-bell shaped transition at the Pt(111)-electrolyte interface[30]. However, this combined model does not include atomic-level details beyond the Helmholtz layer region (mostly due to the size limitations of the computationally expensive AIMD simulations); thus, the full atomic-scale origins of the camel-to-bell shape transition remain elusive.

Using a mean-field quantum mechanics/molecular mechanics (QM/MM) simulation framework, known as density functional theory in classical explicit solvents (DFT-CES)[38–40], we recently reproduced a characteristic camel-shaped curve of an aqueous EDL in the dilute limit[41]. Despite its success in linking the cathodic and anodic peaks with non-monotonic and inflection behaviours in the EDL charging curves, respectively, their molecular origins have not been fully clarified. More importantly, this study was limited to the dilute regime in which only a minimal number of counterions were included to screen the electrode charge. Thus, this approach cannot capture the full complexity of the EDL structural responses under practical, non-dilute conditions, thereby limiting the comprehensive understanding of its potentiodynamic behaviour.

In this study, we investigate the EDL atomic structure as a function of the bulk electrolyte concentration by developing a constant-concentration simulation method, termed Chemostat, which is essential for capturing realistic interfacial behaviours where ion and bulk concentrations can differ by up to 80-fold[42]. Our simulations revealed that the capacitance peaks arise from EDL phase transitions, with a concentration-independent cathodic peak linked to water reorientation at the inner Helmholtz layer (IHL) and a concentration-dependent anodic peak due to anion condensation. The calculated capacitance peak positions match well with the experimental values, successfully reproducing the camel-to-bell shape transition. A full EDL phase diagram was constructed, connecting these transitions to the camel-to-bell shape transition of the capacitance curves, and the predicted water structures were experimentally confirmed using in situ attenuated total reflectance-surface-enhanced infrared absorption spectroscopy (ATR-SEIRAS). We expect that our work will provide a comprehensive picture of the interfacial microenvironment at potentials relevant to practical electrocatalytic applications.

Results and discussion

DFT-CES simulations on the interfaces of Ag(100) and Ag(111) electrodes with the NaF electrolyte are performed by varying σ to evaluate E (Fig. 1a). Here, the results for the Ag(100) electrode are presented unless stated otherwise. During the simulation, the bulk concentration of the electrolyte was controlled using the Chemostat method (Supplementary Fig. 11), producing smoothly varying ion concentration profiles at various electrode potentials (Supplementary Figs. 12–14). Furthermore, the simulation results for finite concentrations are

Table 1 | Comparison of phase transition potentials predicted from all-atom simulations with experimental capacitance peak positions

V_{SHE}	Cathodic peak		Anodic peak	
	Simulation	Experiment	Simulation	Experiment
5 mM (Dilute in simulation)	−0.78	−0.84	−0.47	−0.34
100 mM	−0.78	−0.78	−0.56	−0.49
200 mM	−0.77	−0.78	−0.70	−0.59

Theoretical phase-transition potentials are determined using Maxwell construction lines on the *S*-shaped curves in Fig. 1b, while experimental peak positions are extracted from the capacitance curves in Fig. 1e.

quantitatively consistent with the available experimental data on the potential of zero charge (PZC; −0.63 V_{SHE} for both simulation and experiment) and the interfacial water profile (Supplementary Fig. 15) [43–45].

EDL charging curves (σ-E curves) are calculated for bulk concentrations in the dilute limit (only counter-ions included to neutralise σ), and in the finite value of 0.1 and 0.2 M (Fig. 1b). These curves reveal two noticeable features: a concentration-independent *S*-shaped region in the negative σ (cathodic) region and a concentration-dependent *S*-shaped region in the positive σ (anodic) region. In the *S*-shaped region, a thermodynamic instability exists (refer to Supplementary Note 1 and Supplementary Figs. 1 and 2), causing σ to change along the Maxwell construction line at equilibrium (dashed red line in Fig. 1c), which represents the minimum-free-energy path where two phases coexist. This implies the presence of a first-order phase transition, described using the order parameter σ, which results in capacitance divergence as the potential remains fixed, yielding a capacitance peak (Fig. 1d). Considering EDL charging as a thermodynamic process in which entropy decreases due to electric work (defined by $w = \sigma E$), the peak in $C = \partial\sigma/\partial E$ is analogous to the divergence of the isothermal compressibility $\kappa \sim \partial V/\partial p$ during a liquid-gas phase transition, which is another entropy-decreasing thermodynamic process that is driven by pressure-volume ($w = pV$) work. This argument regarding the phase transition is further supported by the experimental hysteresis observed in the capacitance curves (Supplementary Fig. 16).

Thus, our simulation results indicate the emergence of two capacitance peaks, each associated with a distinct phase transition in the cathodic and anodic regions, respectively. Similarly, the Rotenberg group reported an anomalous capacitance peak driven by structural changes in ionic-liquid-based EDLs[46].

Using the potential corresponding to the Maxwell construction line (i.e., the phase transition potential), we predict the theoretical peak positions at different concentrations and find that they are consistent with experimental values (Fig. 1e), with an error of less than ~0.1 V (Table 1). In the cathodic region, the peak position remains relatively unchanged, whereas in the anodic region, it shifts to lower E values as the bulk concentration increases. Notably, the anodic peak shift is attributed to the development of a more pronounced *S*-shape in the σ-E curve (Fig. 1b), suggesting that stronger thermodynamic instability is induced at higher concentrations (its microscopic origin will be discussed below). Finally, the two peaks merge at high concentrations, resulting in the camel-to-bell shape transition. Same trends were observed for the Ag(111) electrode (Supplementary Fig. 17 and Supplementary Table 1). To the best of our knowledge, this is the first study that reproduces the camel-to-bell shape transition in aqueous EDLs using all-atom simulations.

Water structure reorientation at the cathodic interface

The local charge profiles of cations—the dominant ionic species near the electrode under cathodic potential—reveal the formation of two compact cation layers located at the distances of 5.1 and 7.4 Å from the electrode (Fig. 2a,b and Supplementary Figs. 12–14). These layers are referred to as OHL_1 (the outer Helmholtz layer 1) and OHL_2 (outer Helmholtz layer 2), respectively. The formation of the two OHLs is attributed to the short-range correlation between the solvated cations. Beyond these OHLs, the local cation concentration decays exponentially, which is a typical characteristic of diffuse layers. Thus, our findings suggest the formation of two OHLs and a diffuse layer—distinct from the conventional view based on the GCS model which simplifies the EDL structure by ignoring atomic-level details and ion-ion correlations.

Surprisingly, the net charge profile (including both cationic and anionic contributions) was found to be almost independent of bulk concentration. The net ionic charges that accumulated in OHL_1 and OHL_2 remained nearly the same across different bulk concentrations (Supplementary Note 2 and Supplementary Fig. 4). Furthermore, the fitted exponent of the net charge profile in the diffuse layer, that is the Debye length, was consistently 5.6 Å under all concentration conditions (Supplementary Fig. 18a). The small Debye length suggests substantial electric field screening between the electrode and OHL_1 where a water adlayer exists. This is correlated with the conclusions reached by the Willard group who suggested that water molecules can mute the dependence on ionic strength[47]. The water adlayer effectively screens the field of σ, leading to a similar E. Thus, the capacitance becomes concentration-independent at the cathodic potential. We note that the part of the water adlayer on the electrode surface also participates in solvating the cations in OHL_1, and thus the strong field screening by the water adlayer can similarly occur in other alkali metal cations, as they are hardly desolvated due to their strong ion-dipole interaction[3].

To quantify the water-screening effect, we develop a multi-layer capacitor model consisting of three dielectric layers—ε_1, ε_2, and ε_{DifL}—corresponding to the OHL_1, OHL_2, and diffuse layers, respectively (Fig. 2a). This model can be considered an extended GCS model with additional OHLs. Using the amounts of ions stored in each region obtained from our all-atom simulation, ε_1 and ε_2 are adjusted to reproduce the E values obtained by the simulations (Supplementary Note 2 and Supplementary Figs. 3-6). This yields a positive ε_1 and a negative ε_2 (Fig. 2c). The negative dielectric constant is attributed to the hydrogen-bonding network of interfacial water, which induces an orientationally correlated response to the field and thereby generates an electric field larger than that of the electrode[48]. Moreover, ε_1 exhibits σ-dependent behaviour, reaching a maximum at −13 μC cm^{-2} within the *S*-shape region, indicating the crucial role of water adlayer screening in shaping the cathodic capacitance peak.

As orientational polarisation is the major field-screening mechanism for water, we analysed the orientation of water in the adlayer region at different electrode potentials (Supplementary Fig. 19). At PZC, two distinct peaks are observed in the probability distribution of φ (the angle between the water bisector and the surface normal). The distribution of θ (the angle between the O − H bond and the surface normal) further shows that two water orientations are possible at PZC: (1) both O − H bonds are parallel to the surface, parallel state, and (2) one parallel O − H bond with the other bond pointing toward the bulk region, H-up state. Under a more negative potential, the water orientations converge into a single state, characterised by φ = ~140°, corresponding to a configuration where one O − H bond is parallel and the other points toward the electrode, H-down state.

Based on this three-state classification of the water orientation, which is also consistent with previous studies (see the water configurations in Fig. 2d)[37,41,49], we observed the coexistence of parallel and H-up states at the PZC, stabilised by favourable metal-O(water) interactions and the maximum number of hydrogen bonds. As the electrode potential decreased, a transition to the H-down state was induced (Fig. 2d), driven by the strong interaction between the O − H bond dipole and the electric field from the electrode. As this interaction must overcome the energetic penalty of forming a dangling

https://doi.org/10.1038/s41467-026-70322-5

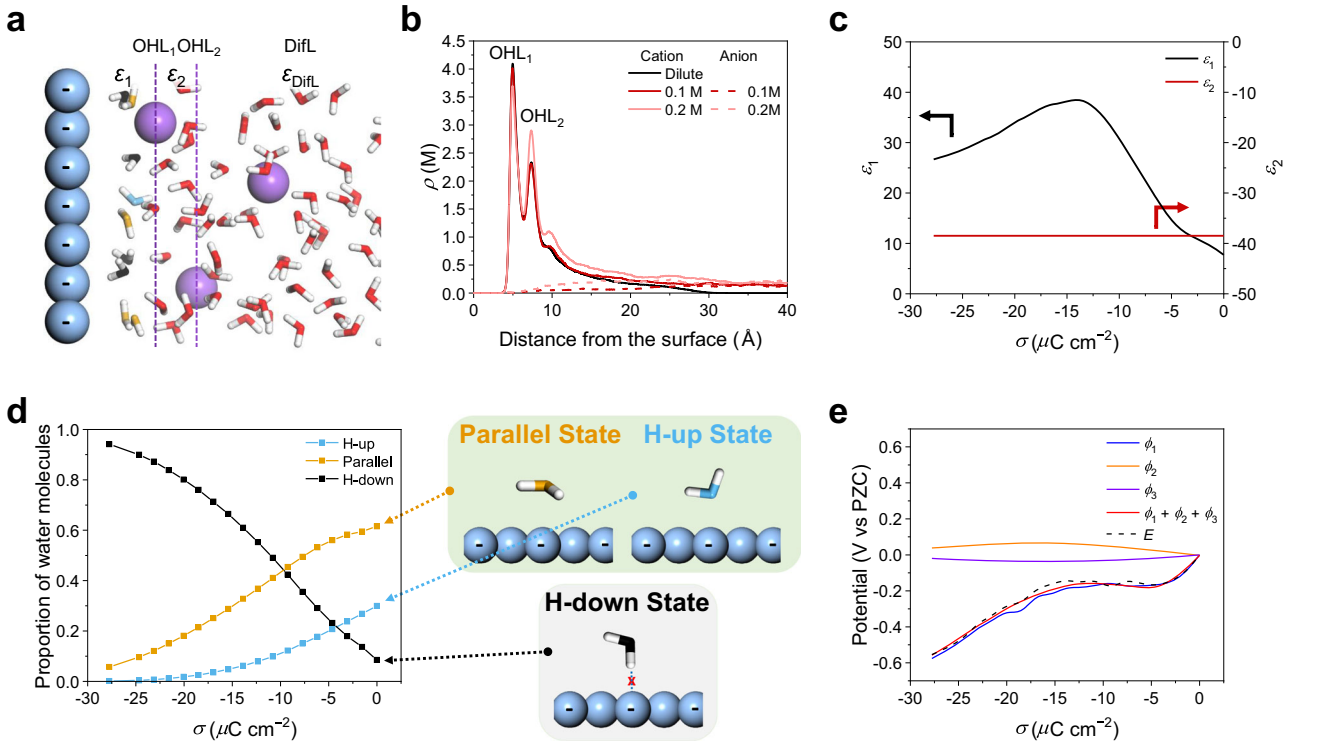

Fig. 2 | Collective reorientation of water molecules driven by cathodic bias. **a** Representative snapshot of the cathodic interface. Hydrogen, sodium, and silver atoms are shown in white, magenta, and blue, respectively. Oxygen atoms in the adlayer are color-coded according to their water orientation state (refer to Fig. 2d), while the other oxygen atoms are shown in red. **b** Local cationic (solid lines) and anionic (dashed lines) charge profiles along the surface normal direction at varying bulk electrolyte concentration ($\sigma = -13.9$ μC cm^{-2}). **c** σ-dependent changes in the dielectric constants, ε_1 for the water between electrode and OHL$_1$, and ε_2 for the water between OHL$_1$ and OHL$_2$, obtained by fitting the multilayer capacitor model to the all-atom simulation results. **d** Populations of water orientation states and their configurations (dilute case). As σ becomes more negative, the populations of the parallel and H-up states decrease, while the population of the H-down state increases. **e** Potential drops between regions: ϕ_1 between electrode and OHL$_1$, ϕ_2 between OHL$_1$ and OHL$_2$, and ϕ_3 between OHL$_2$ and the diffuse layer. This partitioning is achieved by fitting the multi-layer capacitor model to the all-atom simulation results. Note that the sum of ϕ_1, ϕ_2, and ϕ_3 corresponds to the total potential drop across the interface, i.e., the electrode potential with respect to the PZC, $E - E_{PZC}$.

hydrogen bond by restructuring the hydrogen-bond network (Supplementary Fig. 20), the phase transition occurs collectively in a first-order manner (similar to the two-dimensional (2D) spin-1 Ising model; Supplementary Note 3 and Supplementary Figs. 7 and 8). This leads to the non-monotonic behaviour of E as a function of σ (Fig. 2e), giving rise to the capacitance peak[41].

Concentration-dependent anion condensation at the anodic interface

Notably different from the cathodic interface, many anions are adsorbed on the electrode under anodic bias (Fig. 3a)[41] while no dramatic change in the water structure with parallel or H-up state in the IHL is observed (Supplementary Fig. 19). The anion adsorption process is accompanied by the partial desolvation of anions to develop a direct electrostatic interaction with the positively charged electrode, which is facilitated by the dispersion interaction (Supplementary Fig. 21).

The total charge of the adsorbed anions in the IHL (σ_{IHL}) screens σ. Surprisingly, we observe a transition from underscreening ($|\sigma_{IHL}| < \sigma$) to either complete screening or overscreening ($|\sigma_{IHL}| \geq \sigma$) as σ increases (Fig. 3c), with the tendency for overscreening becoming more pronounced at higher bulk concentrations. This concentration-dependent behaviour of the overscreening tendency is related to the distinct EDL structure at the anode compared with the cathode (Supplementary Fig. 18). Since the partially desolvated anions are directly adsorbed on the electrode, the interfacial water adlayer cannot effectively screen the electric field. Consequently, the net charge of the anion-adsorbed electrode ($\sigma + \sigma_{IHL}$) decreases with increasing σ, yielding the S-shaped curve and thereby producing a concentration-dependent peak at the anodic potential. In addition, overscreening causes the net electrode charge to become negative, leading to the formation of two cationic OHLs and a diffuse layer, similar to the structure in the cathodic region (Fig. 3b). This behaviour was also modelled using a multilayer capacitor model consisting of the IHL, OHL$_1$, OHL$_2$, and diffuse layers, as described in Supplementary Note 2.

Although previous studies ascribed the origin of the capacitance peak to ion saturation at the interface (i.e., as a result of repulsion)[34,35], our all-atom simulations showed no evidence of such ion saturation behaviour (Fig. 3c). Rather, the adsorbed anions are closely and quasi-regularly spaced on the electrode surface (Fig. 3d). This unexpected 2D dense ionic structure was observed even at dilute concentrations, implying the presence of an effective attraction that overcomes the strong Coulomb repulsion among the anions. Further analysis reveals that water monomers or dimers bridge adjacent anions in the IHL, maintaining their separation at 3.9 or 6.4 Å, respectively (Fig. 3a).

Since the formation of a 2D dense ionic structure is enabled by effective attraction mediated by water molecules, the anion adsorption process involves anionic condensation, similar to the surface condensation of gas. From this perspective, increasing the bulk concentration lowers the entropy of the gas-like free anions; thus, their condensation into a liquid-like 2D anion layer incurs a lower entropic cost, reducing the work required for the phase transition (Fig. 3e). Consequently, the phase transition potential decreases with increasing concentration.

We further confirm the generalizability of the anion condensation mechanism for NaCl electrolytes, where the simulated anion-condensation potentials correspond well to the experimental peak

https://doi.org/10.1038/s41467-026-70322-5

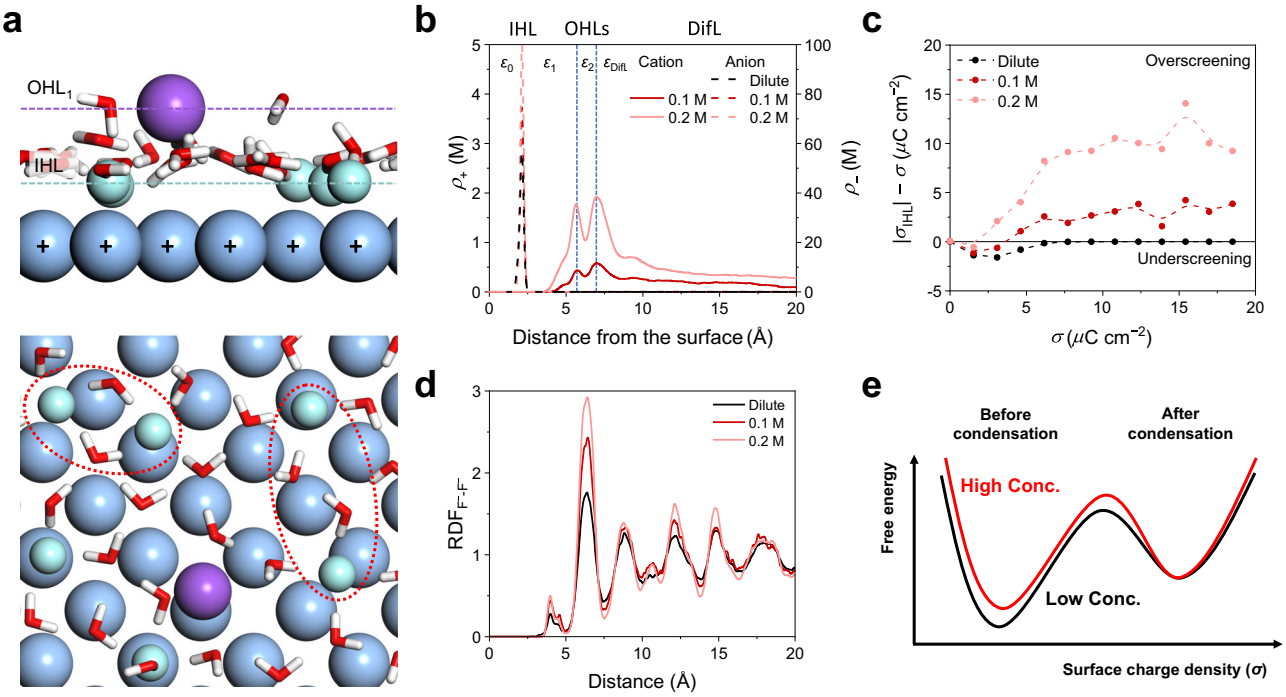

Fig. 3 | Anion surface condensation driven by anodic bias. a Representative snapshot of the anodic interface. Hydrogen, oxygen, fluoride, sodium, and silver atoms are shown in white, red, cyan, magenta, and blue, respectively. Red dashed ovals highlight water-bridging configurations of anions in the IHL. **b** Local cationic (solid lines) and anionic (dashed lines) charge profiles along the surface normal direction at different bulk electrolyte concentrations ($\sigma = 18.5\ \mu C\ cm^{-2}$). **c** σ-dependent variation of the charge difference between the adsorbed anions in the IHL (σ_{IHL}) and σ. The black solid line indicates the condition $|\sigma_{IHL}| = \sigma$, corresponding to complete screening. **d** Radial distribution function (RDF) between anions in the IHL shows intermediate-range ordering among adsorbed anions and is indicative of anion condensation ($\sigma = 18.5\ \mu C\ cm^{-2}$). **e** Schematic free energy diagrams of phase transitions at the anodic interfaces as different bulk concentration. At higher concentrations, the entropy of free (non-adsorbed) ions decreases, destabilising the pre-condensation phase. As a result, the required phase transition potential shifts to a lower value.

positions (Supplementary Figs. 22 and 23, and Supplementary Table 2). When the anion is switched from F^- to Cl^-, the peak positions shift toward smaller anodic potentials, indicating that surface condensation of Cl^- requires a lower energetic cost than that of F^-. This is reasonable because Cl^- has both a lower solvation free energy (F^-: 111.1 kcal mol^{-1}; Cl^-: 81.3 kcal mol^{-1})[50] and a stronger dispersion attraction to the electrode surface (C_6 parameter of F^-: 15.0 a.u.; Cl^-: 30.3 a.u.)[51], facilitating the partial-desolvation-followed-by-surface-adsorption process. This comparative analysis demonstrates that the balance between hydration free energy and dispersion attraction to the electrode plays a decisive role in determining the anion-condensation potential.

Phase diagram of EDL structure

Using the aforementioned multi-layer capacitor models, fine-tuned to reproduce our all-atom simulation results, we inter- and extrapolate the simulated E-σ curves originally obtained at 0, 0.1, and 0.2 M to cover the concentration c range from 0 to 0.3 M (Fig. 4a). Using the multi-layer capacitor model, for a given value of c, we obtain E-σ curves, where the phase transition potentials are determined using Maxwell constructions (Supplementary Fig. 24). This identifies the phase boundaries between phases as a function of c, enabling us to construct a full E-c phase diagram of the EDL structure (Fig. 4b).

The phase diagram of the EDL structure consists of three major phases: the H-down water phase, parallel+H-up water phase, and condensed anion phase (Fig. 4c). At low concentrations (0–0.24 M), increasing the potential from −0.5 to +0.5 V_{PZC} crosses two phase boundaries, implying two phase transitions: first from the H-down water to the parallel+H-up water phase, and then from the parallel+H-up water phase to the condensed anion phase. These transitions give rise to cathodic and anodic peaks, defining the camel-shaped capacitance curve, and the phase boundary between the parallel+H-up water and condensed anion phases is concentration-dependent, accounting for the anodic peak shift with increasing c. For $c > 0.24$ M (triple point), the phase transition occurred directly from the H-down water phase to the anion-condensation phase, resulting in a single peak in the capacitance curve, corresponding to the transition from the camel shape to the bell shape.

Spectroscopic features supporting the EDL phase transition

To identify the spectroscopic features supporting the proposed EDL structural phase transitions, we simulated the infrared (IR) spectra of the interfacial water molecules in the first two layers using DFT calculations (Supplementary Note 4 and Supplementary Fig. 9). At PZC (approximately −0.6 V_{SHE}), the IR spectra for both the dilute and 0.2 M concentrations are dominated by the contributions from the 2nd layer water (~3390 cm^{-1}) and the parallel+H-up water phase in the adlayer (~3380 cm^{-1}; Supplementary Fig. 25 and Supplementary Tables 3 and 4). Using these as references, we observed a reduction in the intensity of the O − H vibrational mode under a cathodic bias (Fig. 5a,b), which is attributed to a decreased population of the parallel+H-up water phase (Fig. 5c), whereas the signals from the 2nd water layer remained largely unchanged. Notably, although the formation of H-down water phase under cathodic bias contributes a signal near ~3340 cm^{-1} (Supplementary Fig. 26), its intensity is weaker due to both a smaller population and the lower transition dipoles (Supplementary Fig. 27). Consequently, this signal is obscured by a more pronounced intensity reduction in the same frequency range.

Under anodic bias, we observe increases in the intensities of two characteristic IR bands at ~3400 and ~3300 cm^{-1} (Fig. 5a,b). These features are attributed to the asymmetric and symmetric stretching

https://doi.org/10.1038/s41467-026-70322-5

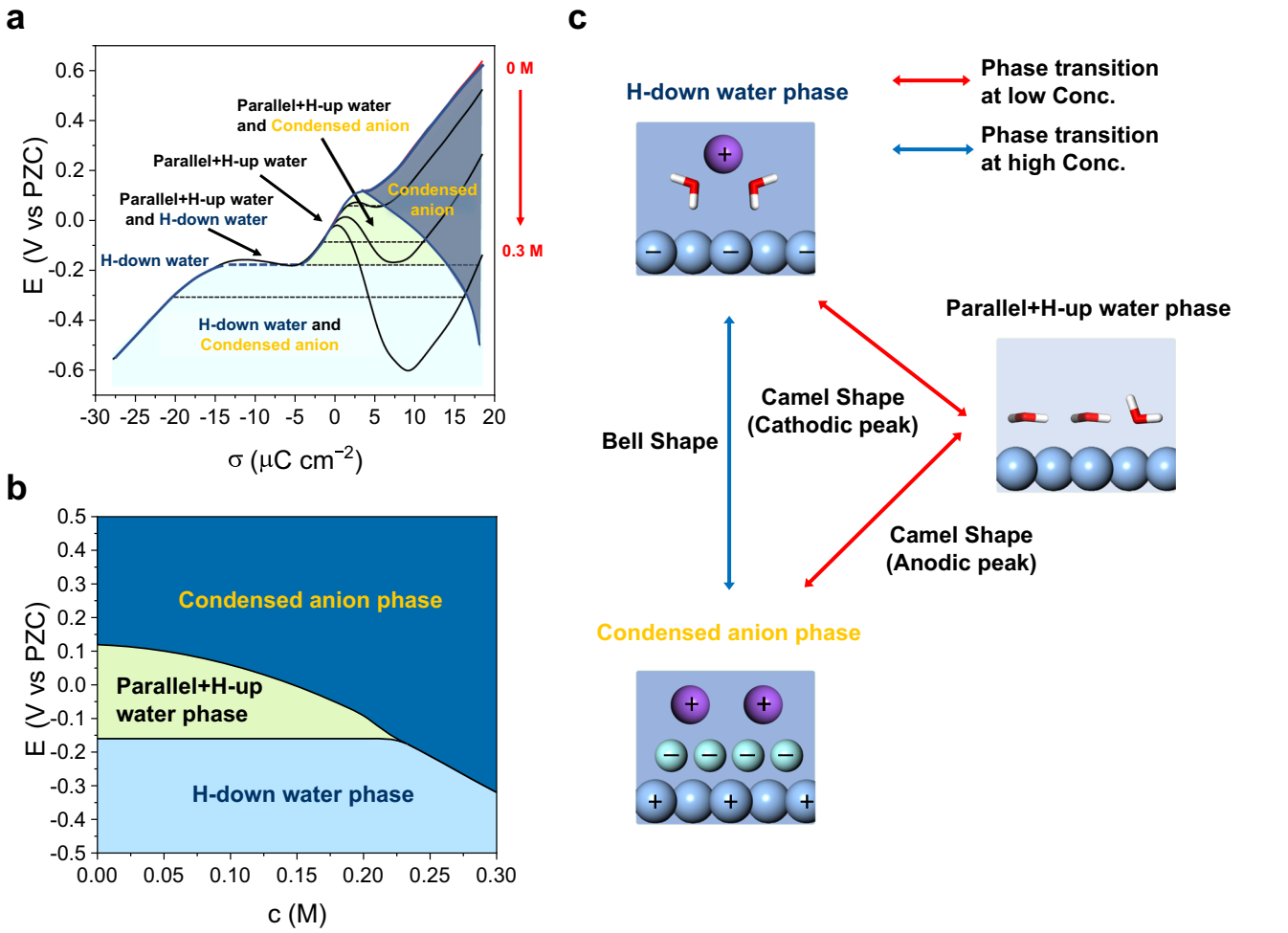

Fig. 4 | Phase diagram of EDL structure and phase transitions. a *E-σ* diagram extended using the multilayer capacitor model fitted to reproduce the all-atom simulation results. **b** *E-c* phase diagram of EDL structure. The number of phase boundary crossings along a vertical line corresponds to the number of phase transitions induced by sweeping the electrode potential, which determines the number of capacitance peaks. **c**, Schematic illustration of the phase transitions between the three EDL structural phases: H-down water phase, parallel+H-up water phase, and condensed anion phase.

modes of water molecules coordinated with F^- anions at the IHL, indicating the formation of the anion-condensed phase. Notably, these spectral increases are more pronounced and emerge at lower bias potentials for the 0.2 M case compared to the dilute regime, reflecting a lower phase transition potential at higher electrolyte concentrations.

These simulated spectral features are supported by the experimental results. In situ ATR-SEIRAS measurements, conducted using an Ag-coated Ge ATR electrode and referenced to the spectrum obtained at −0.6 V_{SHE}, show a decrease in the spectral intensity at approximately 3400 cm^{-1} under cathodic bias in both dilute (5 mM) and concentrated (200 mM) NaF electrolytes (Fig. 5d). Conversely, two IR band intensities increased with anodic bias. Despite broader spectral features—likely resulting from the multi-faceted surface—and the associated uncertainty in spectral deconvolution, the experimentally observed trends are in good agreement with our simulated results within a reasonable error margin (~100 cm^{-1}). More importantly, the experiments also reproduced the trend of stronger anodic spectral features at higher electrolyte concentrations, validating the EDL phase transitions predicted by DFT-CES calculations.

In summary, our study reveals the molecular origins of the capacitance behaviour at electrode-electrolyte interfaces under practical, non-dilute ion concentrations. Using predictive all-atom simulations, we identify two distinct phase transitions: concentration-independent water reorientation in the cathodic region and concentration-sensitive anion condensation in the anodic region. These transitions, whose spectroscopic signatures were also captured in our in situ experiments, give rise to the characteristic camel-to-bell shape evolution of the capacitance curve with increasing ion concentration, a long-standing unresolved phenomenon in the study of EDL. By constructing the EDL phase diagram, we provide a unified framework that relates the interfacial structure, potential, and concentration. These insights deepen our understanding of the EDL microenvironment for electrocatalytic and energy-conversion processes, while also motivating further advances in theory and computation to extend the thermodynamic framework to include complex and non-equilibrium conditions.

Methods

DFT-CES simulations

The mean-field QM/MM simulations were performed using the DFT-CES approach developed by our group, with the incorporation of the Chemostat method. DFT-CES enables accurate sampling of all-atomic information of the EDL. Note that, our DFT-CES method can be related to the DFT-3D-RISM (reference interaction site model) method by replacing the integral-equation solving step to MD sampling[52,53]. The Chemostat method was developed in this study to maintain the bulk concentration of the non-dilute EDL.

In detail, DFT-CES is a mean-field QM/MM simulation method used to accurately describe electrochemical interface systems. In this

https://doi.org/10.1038/s41467-026-70322-5

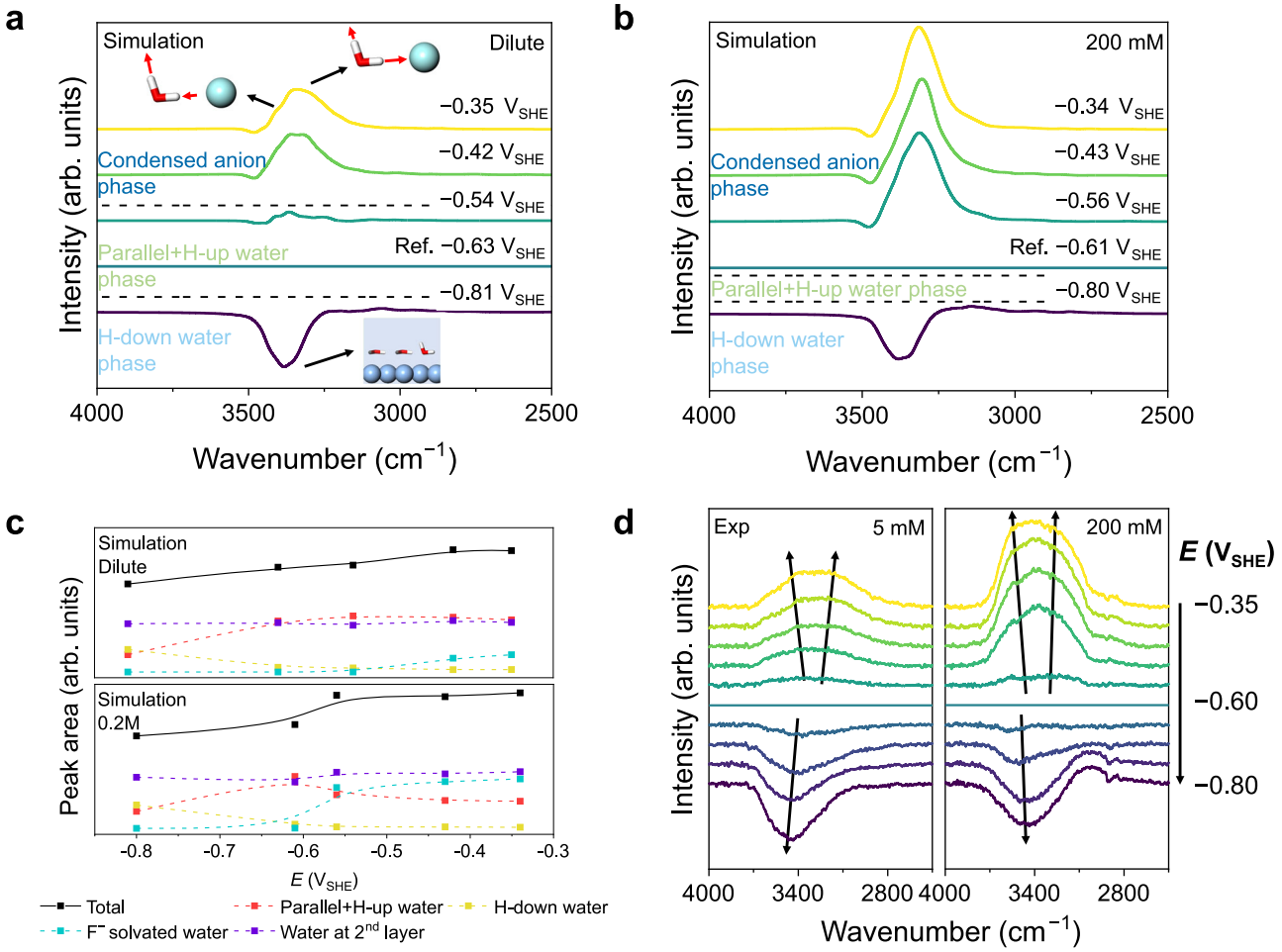

Fig. 5 | Spectroscopic features relevant to the formation of the phases. Calculated IR spectra of interfacial water molecules obtained from DFT-CES trajectories at different bias potentials for (**a**), dilute, and (**b**), 0.2 M bulk concentration conditions. Solid lines show total IR spectra referenced to the spectra at the PZC. Dashed lines indicate the phase transition potentials, with the corresponding phases labelled. Characteristic molecular structures responsible for emerging and disappearing peaks are shown in the inset of (**a**); the same structures also explain the spectral features in (**b**). **c** Integrated peak area for different molecular structures in dilute (top) and 200 mM (bottom) bulk concentration conditions. **d** Experimental ATR-SEIRAS data measured on Ag in 5 and 200 mM NaF electrolytes at 298 K. All experimental spectra are referenced to the spectrum at −0.6 V_{SHE}.

method, QM (mainly for the electrode) and MM (mainly for the electrolyte) simulations are performed iteratively until energy convergence is achieved. The ensemble-averaged electrostatic potential from the MD trajectory was applied as an external potential in the DFT calculations. Conversely, the Hartree and nuclei potentials of the QM subsystem were used as external potentials in the MD simulations. DFT-CES was implemented by combining the Quantum Espresso software for DFT simulations and the large-scale atomic/molecular massive parallel simulator (LAMMPS) software package for MD simulations[54,55].

The Ag(100) and Ag(111) electrodes were interfaced with various bulk concentrations of the electrolyte. Both electrodes were simulated at the QM level. The Ag(100) electrode was modelled using a four-layer slab with the lateral dimensions of 4.14 Å × 4.14 Å. The Ag(111) electrode was modelled using a four-layer slab with a ($\sqrt{3} \times 2$) correct surface unit cell with the dimensions of 5.08 Å × 5.86 Å. The projector-augmented wave (PAW) method was used together with the Perdew-Burke-Ernzerhof (PBE) exchange-correlation functional[56,57]. A kinetic energy cutoff of 60 Ry and Gaussian smearing value of 0.0147 Ry were employed. (9 × 9 × 1)-and (8 × 8 × 1) Γ-centred k-point grids were used for Ag(100) and Ag(111), respectively. A dipole correction along the *z*-direction was applied to cancel the nonphysical interactions between the periodic images.

NaF and NaCl electrolytes were simulated at the MM level using canonical-ensemble classical MD. 6000 TIP3P-EW water molecules[58] were used, and Na^+, F^-, and Cl^- ions were included in the simulation cell. Ion-ion and ion-water interactions were described using parameters reported in the literature[59]. The interfacial van der Waals (vdW) interactions between the NaF electrolyte (in the MM subsystem) and Ag electrode (in the QM subsystem) were described using previously developed first-principles-based parameters that reproduced the experimental camel-shaped capacitance curve of the Ag(111)-NaF interface[41]. For the NaCl electrolyte, the interfacial vdW parameters were fitted to the QM energetics, following the same procedures used for parametrizing the interactions between NaF electrolyte and the Ag electrode (Supplementary Fig. 28 and Supplementary Table 5).

For the dilute case, only the excess Na^+ or F^- (or Cl^-) ions were added to compensate for the excess negative or positive charge of the electrode, respectively. For finite bulk concentration cases, the bulk concentration was maintained at specific values by applying the Chemostat method developed in this study. A detailed description of the Chemostat method is provided in below. For the Ag(100)-NaF (or NaCl) interface, the simulations were performed for the dilute-limit, and 0.1 M and 0.2 M bulk concentrations, whereas for the Ag(111)-NaF interface, the simulations were only performed for the dilute limit and 0.1 M bulk concentrations.

(11 × 11) and (9 × 8) supercells of the small QM cell were employed for the MD simulations of the Ag(100)-NaF (or NaCl) and Ag(111)-NaF interfaces, respectively, resulting in the MD cell sizes of 45.59 Å × 45.59 Å and 45.68 Å × 46.89 Å. The electrodes were polarised by varying the number of electrons, corresponding to the surface charge densities ranging from −27.76 to 18.50 μC cm^{-2} for Ag(100) and from −23.94 to 29.92 μC cm^{-2} for Ag(111). A Nosé-Hoover thermostat was used to maintain the temperature at 300 K with a damping constant of 100 fs[60,61], and periodic boundary conditions (PBCs) were applied along the x- and y-directions. The modified particle-particle particle-mesh (PPPM) method was employed to account for long-range electrostatic interactions in the slab geometry[62]. Canonical ensemble simulations were performed for 12 ns, and the final 10 ns of the trajectory were used to compute the ensemble properties.

The electrode potential was calculated using the scheme proposed by Trasatti[63], in which the absolute potential of the standard hydrogen electrode (SHE) is set to 4.4 V[41,64]. The electrode potential relative to the SHE is given by:

$$E\left(V_{\mathrm{SHE}}\right) = E_{\mathrm{vac}} - E_F - 4.4\,V \tag{1}$$

where E_{vac} is the vacuum level and E_F is the Fermi level.

In this study, we developed a Chemostat method that efficiently and stably controls the bulk concentration of interfacial systems during MD simulations. To establish the Chemostat method, we first chose the bulk region, which must be sufficiently distant from the interface, such that the local concentrations of both cations and anions are equal and spatially uniform (Supplementary Fig. 29).

During MD simulation, the local ion concentration in the bulk region, $C(t)$, was calculated for each snapshot at time t. The Chemostat method determines the concentration adjustment rate as follows:

$$\frac{dC}{dt} = \frac{C^0 - C}{\tau} \tag{2}$$

where C^0 is the target concentration and τ is the Chemostat coupling constant, which determines the time scale of the adjustment. Equation (2) is equivalent to the governing equation of the Berendsen thermostat[65] used to control the temperature. In this study, τ was set to 1 ps.

The Chemostat adjusts $C(t)$ by modifying the partial charges of a tagged ion pair located within the bulk region. Based on the computed dC/dt value from Eq. (2), the Chemostat determines the (de)growth rate of the tagged ion pair. To (de)grow ions while avoiding close contact with the existing molecules in the simulation cell, soft-core potentials were employed for the van der Waals (u_{LJ}) and Coulomb (u_{Coul}) interactions[66]:

$$u_{\mathrm{LJ}}(r,\lambda) = \lambda 4\epsilon\left\{\frac{1}{\left[\alpha_{LJ}(1-\lambda)^2 + \left(\frac{r}{\sigma}\right)^s\right]^{\frac{12}{s}}} - \frac{1}{\left[\alpha_{LJ}(1-\lambda)^2 + \left(\frac{r}{\sigma}\right)^s\right]^{\frac{6}{s}}}\right\} \tag{3}$$

$$u_{\mathrm{Coul}}(r,\lambda) = \lambda\frac{q_i q_j}{4\pi\epsilon_0\left[\alpha_{\mathrm{Coul}}(1-\lambda)^2 + r^p\right]^{\frac{1}{p}}} \tag{4}$$

where $s = 2$, $p = 2$, $\alpha_{\mathrm{LJ}} = 6.25/\sigma^2$, and $\alpha_{\mathrm{Coul}} = 6.25$. The activation parameter, λ gradually switches on the interaction as it changes from 0 to 1.

Using Eq. (2), the change in the concentration, defined as $\Delta C(t) \equiv C(t+\Delta t) - C(t)$, over an MD timestep, Δt, is expressed as:

$$\Delta C(t) = \frac{\left(C^0 - C(t)\right)\Delta t}{\tau} \tag{5}$$

For ions, this change leads to

$$\Delta\lambda(t) = \frac{V_{\mathrm{bulk}}\Delta C(t)}{N_A} \tag{6}$$

where V_{bulk} is the volume of the bulk region and N_A is Avogadro's constant, as we used the molarity unit for concentration. Using Eq. (6), we (de)grow the tagged ion pairs. When $\lambda < 0$, the originally tagged ion pair is deleted, and a new ion pair in the bulk region is selected, with its activation parameter set to $\lambda + 1$. When $\lambda > 0$, the tagged ion pair is fully grown (i.e., $\lambda = 1$) and can then freely travel throughout the simulation cell without being confined to the bulk region. Then, a new ion pair in the bulk region is created, and its activation parameter is set to $\lambda - 1$. We confirmed that the bulk concentration was well-maintained using the Chemostat method not only for monovalent ions but also for multivalent ions (Supplementary Figs. 29 and 30).

Although the Eq. (5) is formally similar to Berendsen-type thermo- or barostats, we note that it maintains the total number of ion-pairs in the bulk region of the simulation cell without disrupting the correct ensemble distributions. To ensure that our simulation, employing a Nosé-Hoover thermostat, correctly samples the canonical ensemble, we confirmed that the particle velocity distribution follows the Maxwell-Boltzmann distribution (Supplementary Fig. 31).

Electrochemical measurements

Electrochemical measurements were performed using an SP−150 potentiostat (BioLogic) in a custom-made (polyetheretherketone) H-type electrochemical cell. Prior to each measurement, the cell was cleaned by sequential boiling in 0.5 M H_2SO_4 (98%, Daejung) and deionised (DI) water (>18.2 MΩ·cm, Arium® Pro, Sartorius) over 3 h. Single-crystalline Ag foils with (111) and (100) orientations (1 × 1 cm^2, 99.999%, MTI) were used as working electrodes. The Ag electrodes were chemically polished using a previously reported procedure[67–69]. Briefly, each electrode was immersed in a mixed solution of 0.3 M KCN (≥96%, Sigma-Aldrich) and H_2O_2 (29–32%, Alfa Aesar) at a volume ratio of 1.5:1 for 3 s, during which vigorous gas evolution occurred. The electrode was then exposed to air for an additional 3 s, followed by immersion in a 0.55 M KCN solution until gas evolution ceased. The electrode was then thoroughly rinsed with DI water. This polishing cycle was repeated 8–12 times to obtain a highly reflective surface. Prior to use, the polished Ag surface was protected using a water droplet.

The differential capacitance was measured using staircase potentiostatic electrochemical impedance spectroscopy (SPEIS). A graphite rod and saturated Ag/AgCl electrode (RE-1A, EC-Frontier) served as the counter and reference electrodes, respectively. The geometric area of the working electrode exposed to the electrolyte was limited to 0.16 cm^2. Electrolytes were prepared by dissolving NaF (~99%, Sigma-Aldrich) in DI water. To prevent unexpected contamination, the working electrode was spatially separated from the counter and reference compartments using a Nafion 115 membrane (DuPont). Measurements were conducted over a potential range from −1.1 to 0 V_{SHE} at a frequency of 20 Hz with a potential amplitude of 10 mV. All measurements were carried out in a deaerated electrolyte under continuous Ar (99.999%, Donghae Gas Ind.) flow. The ohmic drop was manually compensated by 85% during the SPEIS experiments. The experiments were performed at 298 ± 1 K without the use of an environmental chamber.

In situ ATR-SEIRAS measurements

Chemically deposited Ag films were prepared by immersing a Ge substrate (60° angle, 20 mm radius; PIKE Technologies) into a mixed solution consisting of a hydrazine solution (50 µL, 0.02 M) and a silver nitrate solution (10 mL, 0.01 M) containing ammonium hydroxide (0.46 M) and EDTA (0.14 M)[70]. The deposition was conducted for 150 s.

Following the deposition, the substrate was thoroughly rinsed with DI water and dried under Ar atmosphere. In situ ATR-SEIRAS measurements were performed using a Nicolet iS50 FTIR spectrometer (Thermo Fisher Scientific) equipped with a liquid-nitrogen-cooled mercury cadmium telluride (MCT) detector. To eliminate interference from ambient water vapour and CO_2, the entire optical path was purged with high-purity N_2 (99.999% purity, Donghae Gas Ind.). Spectra were collected using a specular reflection unit (VeeMax III, PIKE Technologies) equipped with a Ge ATR prism and a light polariser, with the incident angle fixed at 60°. The measurements were performed at a spectral resolution of 8 cm^{-1} by averaging 128 scans per spectrum. A spectrochemical flow-type cell was mounted on the Ge prism, with the Ag-coated Ge surface serving as the working electrode (exposed geometric area of 0.5 cm^2). A silver wire and saturated Ag/AgCl electrode were used as the counter and reference electrodes, respectively. Electrolytes were 5 and 200 mM NaF. Prior to gathering IR spectra, the surface of working electrode was cleaned by 100 cycles of cyclic voltammetry from −0.9 V to 0.0 V_{SHE} at a scan rate of 200 mV s^{-1}. All spectra are presented relative to a reference spectrum recorded at −0.6 V_{SHE}, a potential close to the PZC. The experiments were performed at 298 ± 1 K without the use of an environmental chamber.

Data availability

All computational data generated in this study are provided via the Zenodo database at https://doi.org/10.5281/zenodo.16730327[71]. Source data are provided with this paper.

Code availability

The modified LAMMPS code with the Chemostat method has been deposited in the Zenodo database without an accession code at https://doi.org/10.5281/zenodo.18679493[72].

References

1. Helmholtz, H. Ueber einige Gesetze der Vertheilung elektrischer Ströme in körperlichen Leitern mit Anwendung auf die thierisch-elektrischen Versuche. *Ann. Phys.* **165**, 211–233 (1853).
2. Schmickler, W. Double layer theory. *J. Solid State Electrochem.* **24**, 2175–2176 (2020).
3. Ringe, S. et al. Understanding cation effects in electrochemical CO_2 reduction. *Energy Environ. Sci.* **12**, 3001–3014 (2019).
4. Ringe, S. et al. Double layer charging driven carbon dioxide adsorption limits the rate of electrochemical carbon dioxide reduction on gold. *Nat. Commun.* **11**, 33 (2020).
5. Monteiro, M. C. O. et al. Absence of CO_2 electroreduction on copper, gold and silver electrodes without metal cations in solution. *Nat. Catal.* **4**, 654–662 (2021).
6. Monteiro, M. C. O., Goyal, A., Moerland, P. & Koper, M. T. M. Understanding cation trends for hydrogen evolution on platinum and gold electrodes in alkaline media. *ACS Catal.* **11**, 14328–14335 (2021).
7. Shin, S.-J. et al. A unifying mechanism for cation effect modulating C1 and C2 productions from CO_2 electroreduction. *Nat. Commun.* **13**, 5482 (2022).
8. Ji, S. G. et al. Alkali metal cations act as homogeneous cocatalysts for the oxygen reduction reaction in aqueous electrolytes. *Nat. Catal.* **7**, 1330–1338 (2024).
9. Kim, H. et al. Cation effect on the electrochemical platinum dissolution. *J. Am. Chem. Soc.* **147**, 4667–4674 (2025).
10. Liu, E. et al. Interfacial water shuffling the intermediates of hydrogen oxidation and evolution reactions in aqueous media. *Energy Environ. Sci.* **13**, 3064–3074 (2020).
11. Huang, B. et al. Cation- and pH-dependent hydrogen evolution and oxidation reaction kinetics. *JACS Au* **1**, 1674–1687 (2021).
12. Malkani, A. S. et al. Understanding the electric and non-electric field components of the cation effect on the electrochemical CO reduction reaction. *Sci. Adv.* **6**, eabd2569 (2020).
13. Shah, A. H. et al. The role of alkali metal cations and platinum-surface hydroxyl in the alkaline hydrogen evolution reaction. *Nat. Catal.* **5**, 923–933 (2022).
14. Resasco, J. et al. Promoter effects of alkali metal cations on the electrochemical reduction of carbon dioxide. *J. Am. Chem. Soc.* **139**, 11277–11287 (2017).
15. Goyal, A. & Koper, M. T. M. The interrelated effect of cations and electrolyte pH on the hydrogen evolution reaction on gold electrodes in alkaline media. *Angew. Chem. Int. Ed.* **60**, 13452–13462 (2021).
16. Jiao, L., Liu, E., Mukerjee, S. & Jia, Q. In situ identification of non-specific adsorption of alkali metal cations on Pt surfaces and their catalytic roles in alkaline solutions. *ACS Catal.* **10**, 11099–11109 (2020).
17. Monteiro, M. C. O., Dattila, F., López, N. & Koper, M. T. M. The role of cation acidity on the competition between hydrogen evolution and CO_2 reduction on gold electrodes. *J. Am. Chem. Soc.* **144**, 1589–1602 (2022).
18. Ovalle, V. J., Hsu, Y. S., Agrawal, N., Janik, M. J. & Waegele, M. M. Correlating hydration free energy and specific adsorption of alkali metal cations during CO_2 electroreduction on Au. *Nat. Catal.* **5**, 624–632 (2022).
19. Malkani, A. S., Anibal, J. & Xu, B. Cation effect on interfacial CO_2 concentration in the electrochemical CO_2 reduction reaction. *ACS Catal.* **10**, 14871–14876 (2020).
20. Zhang, F. & Co, A. C. Direct evidence of local pH change and the role of alkali cation during CO_2 electroreduction in aqueous media. *Angew. Chem. Int. Ed.* **59**, 1674–1681 (2020).
21. Singh, M. R., Kwon, Y., Lum, Y., Ager, J. W. & Bell, A. T. Hydrolysis of electrolyte cations enhances the electrochemical reduction of CO_2 over Ag and Cu. *J. Am. Chem. Soc.* **138**, 13006–13012 (2016).
22. Subbaraman, R. et al. Enhancing hydrogen evolution activity in water splitting by tailoring Li^+-$Ni(OH)_2$-Pt Interfaces. *Science* **334**, 1256–1260 (2011).
23. Strmcnik, D. et al. The role of non-covalent interactions in electrocatalytic fuel-cell reactions on platinum. *Nat. Chem.* **1**, 466–472 (2009).
24. Li, J. et al. Hydroxide is not a promoter of C_{2+} product formation in the electrochemical reduction of CO on Copper. *Angew. Chem. Int. Ed.* **132**, 4494–4499 (2020).
25. Murata, A. & Hori, Y. Product selectivity affected by cationic species in electrochemical reduction of CO_2 and CO at a Cu electrode. *Bull. Chem. Soc. Jpn.* **64**, 123–127 (1991).
26. Grahame, D. C. The electrical double layer and the theory of electrocapillarity. *Chem. Rev.* **41**, 441–501 (1947).
27. Valette, G. Double layer on silver single-crystal electrodes in contact with electrolytes having anions which present a slight specific adsorption Part I. The (110) face. *J. Electroanal. Chem. Interfacial Electrochem.* **122**, 285–297 (1981).
28. Valette, G. Double layer on silver single crystal electrodes in contact with electrolytes having anions which are slightly specifically adsorbed Part II. The (100) face. *J. Electroanal. Chem. Interfacial Electrochem.* **138**, 37–54 (1982).
29. Valette, G. Double layer on silver single crystal electrodes in contact with electrolytes having anions which are slightly specifically adsorbed Part III. The (111) face. *J. Electroanal. Chem. Interfacial Electrochem.* **269**, 191–203 (1989).
30. Ojha, K., Doblhoff-Dier, K. & Koper, M. T. M. Double-layer structure of the Pt(111)–aqueous electrolyte interface. *Proc. Natl. Acad. Sci. USA* **119**, e2116016119 (2022).
31. Gouy, M. Sur la constitution de la charge électrique à la surface d'un électrolyte. *J. Phys.: Theor. Appl.* **9**, 457–468 (1910).

32. Chapman, D. L. LI. A contribution to the theory of electrocapillarity. *Lond. Edinb. Philos. Mag. J. Sci.* **25**, 475–481 (1913).
33. Stern, O. Zur theorie der elektrolytischen doppelschicht. *Zeit Elektrochem.* **30**, 508–516 (1924).
34. Kornyshev, A. A. Double-layer in ionic liquids: paradigm change? *J. Phys. Chem. B* **111**, 5545–5557 (2007).
35. Shatla, A. S., Landstorfer, M. & Baltruschat, H. On the differential capacitance and potential of zero charge of Au(111) in some aprotic solvents. *ChemElectroChem* **8**, 1817–1835 (2021).
36. Huang, J. Density-potential functional theory of electrochemical double layers: calibration on the Ag(111)-KPF_6 system and parametric analysis. *J. Chem. Theory Comput.* **19**, 1003–1013 (2023).
37. Le, J.-B., Fan, Q.-Y., Li, J.-Q. & Cheng, J. Molecular origin of negative component of Helmholtz capacitance at electrified Pt(111)/water interface. *Sci. Adv.* **6**, eabb1219 (2020).
38. Lim, H. K., Lee, H. & Kim, H. A seamless grid-based interface for mean-field QM/MM coupled with efficient solvation free energy calculations. *J. Chem. Theory Comput.* **12**, 5088–5099 (2016).
39. Jang, T., Paik, D., Shin, S. & Kim, H. Density functional theory in classical explicit solvents: mean-field QM/MM method for simulating solid–liquid interfaces. *Bull. Korean Chem. Soc.* **43**, 476–483 (2022).
40. Zhang, C. et al. 2023 roadmap on molecular modelling of electrochemical energy materials. *J. Phys. Energy* **5**, 041501 (2023).
41. Shin, S.-J. et al. On the importance of the electric double layer structure in aqueous electrocatalysis. *Nat. Commun.* **13**, 174 (2022).
42. Garlyyev, B., Xue, S., Watzele, S., Scieszka, D. & Bandarenka, A. S. Influence of the nature of the alkali metal cations on the electrical double-layer capacitance of model Pt(111) and Au(111) electrodes. *J. Phys. Chem. Lett.* **9**, 1927–1930 (2018).
43. Toney, M. F. et al. Voltage-dependent ordering of water molecules at an electrode–electrolyte interface. *Nature* **368**, 444–446 (1994).
44. Karl, R. M. et al. Charge-induced equilibrium dynamics and structure at the Ag(001)-electrolyte interface. *Phys. Chem. Chem. Phys.* **17**, 16682–16687 (2015).
45. Kasina, A., Cocklin, E., Horswell, S., Grunder, Y. & Lucas, C. A. Structure of the electrochemical interface: Ag(hkl) in an alkaline electrolyte. *J. Phys. Chem. C.* **128**, 13318–13332 (2024).
46. Merlet, C. et al. The electric double layer has a life of its own. *J. Phys. Chem. C.* **118**, 18291–18298 (2014).
47. Limaye, A., Suvlu, D. & Willard, A. P. Water molecules mute the dependence of the double-layer potential profile on ionic strength. *Faraday Discuss* **249**, 267–288 (2023).
48. Tran, B., Zhou, Y., Janik, M. J. & Milner, S. T. Negative dielectric constant of water at a metal interface. *Phys. Rev. Lett.* **131**, 248001 (2023).
49. Le, J., Cuesta, A. & Cheng, J. The structure of metal-water interface at the potential of zero charge from density functional theory-based molecular dynamics. *J. Electroanal. Chem.* **819**, 87–94 (2018).
50. Marcus, Y. Thermodynamics of Solvation of Ions. Part 5. Gibbs free energy of hydration at 298.15 K. *J. Chem. Soc., Faraday Trans.* **87**, 2995–2999 (1991).
51. Gould, T. & Bučko, T. C_6 coefficients and dipole polarizabilities for all atoms and many ions in rows 1–6 of the periodic table. *J. Chem. Theory Comput.* **12**, 3603–3613 (2016).
52. Nishihara, S. & Otani, M. Hybrid solvation models for bulk, interface, and membrane: reference interaction site methods coupled with density functional theory. *Phys. Rev. B* **96**, 115429 (2017).
53. Hagiwara, S., Nishihara, S., Kuroda, F. & Otani, M. Development of a dielectrically consistent reference interaction site model combined with the density functional theory for electrochemical interface simulations. *Phys. Rev. Mater.* **6**, 093802 (2022).
54. Plimpton, S. Fast parallel algorithms for short-range molecular dynamics. *J. Comput. Phys.* **117**, 1–19 (1995).
55. Giannozzi, P. et al. QUANTUM ESPRESSO: a modular and open-source software project for quantum simulations of materials. *J. Phys. Condens. Matter* **21**, 395502 (2009).
56. Blöchl, P. E. Projector augmented-wave method. *Phys. Rev. B* **50**, 17953–17979 (1994).
57. Perdew, J. P., Burke, K. & Ernzerhof, M. Generalized gradient approximation made simple. *Phys. Rev. Lett.* **77**, 3865–3868 (1996).
58. Price, D. J. & Brooks, C. L. A modified TIP3P water potential for simulation with Ewald summation. *J. Chem. Phys.* **121**, 10096–10103 (2004).
59. Fyta, M. & Netz, R. R. Ionic force field optimization based on single-ion and ion-pair solvation properties: going beyond standard mixing rules. *J. Chem. Phys.* **136**, 124103 (2012).
60. Nosé, S. A unified formulation of the constant temperature molecular dynamics methods. *J. Chem. Phys.* **81**, 511–519 (1984).
61. Hoover, W. G. Canonical dynamics: equilibrium phase-space distributions. *Phys. Rev. A* **31**, 1695–1697 (1985).
62. Pollock, E. L. & Glosli, J. Comments on P^3M, FMM, and the Ewald method for large periodic coulombic systems. *Comput. Phys. Commun.* **95**, 93–110 (1996).
63. Trasatti, S. The absolute electrode potential: An explanatory note. *Pure Appl. Chem.* **58**, 955–966 (1986).
64. Le, J., Iannuzzi, M., Cuesta, A. & Cheng, J. Determining potentials of zero charge of metal electrodes versus the standard hydrogen electrode from density-functional-theory-based molecular dynamics. *Phys. Rev. Lett.* **119**, 016801 (2017).
65. Berendsen, H. J. C., Postma, J. P. M., van Gunsteren, W. F., DiNola, A. & Haak, J. R. Molecular dynamics with coupling to an external bath. *J. Chem. Phys.* **81**, 3684–3690 (1984).
66. Moučka, F. et al. Molecular simulation of aqueous electrolyte solubility. 2. Osmotic ensemble Monte Carlo methodology for free energy and solubility calculations and application to NaCl. *J. Phys. Chem. B* **115**, 7849–7861 (2011).
67. Jovićević, J. N., Jović, V. D. & Despić, A. R. The influence of adsorbing substances on the lead UPD onto (111) oriented silver single crystal surface—I. *Electrochim. Acta* **29**, 1625–1638 (1984).
68. Bewick, A. & Thomas, B. Optical and electrochemical studies of the underpotential deposition of metals Part I. Thallium deposition on single crystal silver electrodes. *J. Electroanal. Chem.* **65**, 911–931 (1975).
69. Adzic, R. R., Hanson, M. E. & Yeager, E. B. Structure of silver (100) and (111) single-crystal surfaces obtained by chemical polishing. *J. Electrochem. Soc.* **131**, 1730–1731 (1984).
70. Delgado, J. M., Orts, J. M. & Rodes, A. ATR-SEIRAS study of the adsorption of acetate anions at chemically deposited silver thin film electrodes. *Langmuir* **21**, 8809–8816 (2005).
71. Kim, M. M. et al. Electric double layer structure in concentrated aqueous solution, Zenodo repository, https://doi.org/10.5281/zenodo.16730327 (2026).
72. Kim, M. M. et al. Electric double layer structure in concentrated aqueous solution, Zenodo repository, https://doi.org/10.5281/zenodo.18679493 (2026).

Acknowledgements

This research was supported by the Samsung Science and Technology Foundation (Grant No. SSTF-BA2101-08 (M.M.K., D.H.K., J.C., H.K., and C.H.C.)), and National Research Foundation of Korea funded by the Korean government (Grant No. RS-2024-00435493 to M.M.K. and H.K., and Grant No. RS-2025-25442300 to D.H.K., J.C., S.-J.S., and C.H.C.). It was also supported by the InnoCORE program of the Ministry of Science and ICT (1.260005.01).

Author contributions

H.K. and S.-J.S. conceived the initial idea and H.K., C.H.C., and S.-J.S. supervised the project. M.M.K. performed the DFT-CES simulations and

analysed the data. D.H.K. and J.C. performed the SPEIS and ATR-SEIRAS experiments, respectively. M.M.K., D.H.K., and J.C. contributed equally. All authors have written and revised the manuscript.

Competing interests

The authors declare no competing interests.

Additional information

Supplementary information The online version contains supplementary material available at https://doi.org/10.1038/s41467-026-70322-5.

Correspondence and requests for materials should be addressed to Seung-Jae Shin, Chang Hyuck Choi or Hyungjun Kim.

Peer review information *Nature Communications* thanks Sung Sakong, Wen-Bin Cai, Bingjun Xu and the other, anonymous, reviewer(s) for their contribution to the peer review of this work. A peer review file is available.